PNAS RESEARCH ARTICLE | EARTH, ATMOSPHERIC, AND PLANETARY SCIENCES OPEN ACCESS

Seismic detection of a deep mantle discontinuity within Mars by InSight

Quancheng Huang[a,b,1], Nicholas C. Schmerr[a], Scott D. King[c], Doyeon Kim[a,d], Attilio Rivoldini[e], Ana-Catalina Plesa[f], Henri Samuel[g], Ross R. Maguire[a], Foivos Karakostas[a,h], Vedran Lekić[a], Constantinos Charalambous[i], Max Collinet[f], Robert Myhill[j], Daniele Antonangeli[k], Mélanie Drilleau[l], Misha Bystricky[m], Caroline Bollinger[m], Chloé Michaut[n], Tamara Gudkova[o], Jessica C. E. Irving[j], Anna Horleston[i], Benjamin Fernando[p], Kuangdai Leng[p], Tarje Nissen-Meyer[p], Frederic Bejina[m], Ebru Bozdağ[b], Caroline Beghein[q], Lauren Waszek[r], Nicki C. Siersch[k], John-Robert Scholz[s], Paul M. Davis[q], Philippe Lognonné[g], Baptiste Pinot[l], Rudolf Widmer-Schnidrig[t], Mark P. Panning[u], Suzanne E. Smrekar[u], Tilman Spohn[f], William T. Pike[i], Domenico Giardini[d], and W. Bruce Banerdt[u]

Edited by Michael Manga, University of California, Berkeley, CA; received March 23, 2022; accepted September 1, 2022

Constraining the thermal and compositional state of the mantle is crucial for deciphering the formation and evolution of Mars. Mineral physics predicts that Mars' deep mantle is demarcated by a seismic discontinuity arising from the pressure-induced phase transformation of the mineral olivine to its higher-pressure polymorphs, making the depth of this boundary sensitive to both mantle temperature and composition. Here, we report on the seismic detection of a midmantle discontinuity using the data collected by NASA's InSight Mission to Mars that matches the expected depth and sharpness of the postolivine transition. In five teleseismic events, we observed triplicated P and S waves and constrained the depth of this discontinuity to be 1,006 ± 40 km by modeling the triplicated waveforms. From this depth range, we infer a mantle potential temperature of 1,605 ± 100 K, a result consistent with a crust that is 10 to 15 times more enriched in heat-producing elements than the underlying mantle. Our waveform fits to the data indicate a broad gradient across the boundary, implying that the Martian mantle is more enriched in iron compared to Earth. Through modeling of thermochemical evolution of Mars, we observe that only two out of the five proposed composition models are compatible with the observed boundary depth. Our geodynamic simulations suggest that the Martian mantle was relatively cold 4.5 Gyr ago (1,720 to 1,860 K) and are consistent with a present-day surface heat flow of 21 to 24 mW/m^2.

interior of Mars | mantle transition zone | thermal evolution of Mars

Significance

The depth and sharpness of a midmantle seismic discontinuity, associated with the phase transition from mineral olivine to its higher-pressure polymorphs, provide essential clues to understanding the temperature and composition of Martian mantle. Using data from NASA's InSight mission, we examined five marsquakes located 3,400 to 4,400 km away from the InSight lander and observed triplications of the P and S waves that resulted from the interaction with a seismic discontinuity produced by the postolivine transition. Our observations indicate that the Martian mantle is more iron rich than Earth,and both planets have a similar potential temperature. Our geodynamic modeling further constrains the mantle composition and surface heat flow and indicates that the mantle was cold in the early Noachian.

Mars, like other terrestrial planets, formed through the accretion of planetesimals into a rocky planet and further differentiated into crust, mantle, and core (1). However, due to the absence of plate tectonics, Mars retains signatures of early processes within its basic inner structural parameters, such as the size, state, and composition of the core, and the composition and layering of the mantle. Thus, understanding the interior structure of Mars sheds light on the formation and evolution of the terrestrial planets.

Planetary seismology provides an in situ method to directly constrain the Martian interior structure from seismic waves (2). In November 2018, NASA's Interior Exploration using Seismic Investigations, Geodesy and Heat Transport (InSight) mission landed in Elysium Planitia on Mars, deploying the Seismic Experiment for Interior Structure (SEIS) seismometers to the surface (3, 4). One of the primary scientific objectives of the InSight mission is to determine the structure, composition, and thermal state of the Martian interior (5–8). After nearly two Martian years of operation, SEIS has detected over 1,000 seismic events (9), establishing that Mars is seismically active (10). These seismic data have revealed the crustal thickness and layering beneath the InSight lander (4, 11) and provided constraints on upper mantle structure (12) and core radius of Mars (13), as well as the seismicity rate on Mars (10).

Previous composition models of Mars were largely constructed using geochemical data from Martian meteorites and chondrites (14–20), in combination with orbital geophysical data such as mass, moment of inertia (MoI), and tidal Love number (21). Starting from these composition models, theoretical seismic profiles of the Martian interior can be modeled with internally consistent thermodynamic approaches and assumed temperature profiles from geodynamic simulations (22). Such an approach has been recently shown to provide seismic velocities within a few percent of actual measurements on Martian mineralogical assemblages at pressure and temperature conditions directly pertinent to Mars' shallow mantle and midmantle (23). In these models, a seismic discontinuity associated with the pressure-induced phase change from olivine to

The authors declare no competing interest.

This article is a PNAS Direct Submission.

[1]To whom correspondence may be addressed. Email: qchuang@umd.edu.

This article contains supporting information online at http://www.pnas.org/lookup/suppl/doi:10.1073/pnas.2204474119/-/DCSupplemental.

Published October 10, 2022.

its polymorphs (24–26), including wadsleyite and ringwoodite, is predicted to exist at 950 to 1,150 km depth. This interface corresponds to the 410-km discontinuity on Earth that delineates the top of the mantle transition zone (MTZ) (27). Due to the expected higher iron content of the Martian mantle and the complexity of the phase diagram, at low-temperature conditions, olivine would first transform into ringwoodite and then to wadsleyite as pressure increases, whereas at high-temperature conditions, olivine would transform into wadsleyite directly, before the stabilization of ringwoodite at further high pressures (24). Given this entangled behavior, we simply refer to these phase transitions as the postolivine transitions hereafter and investigate the possibility of both structures. Notably, Mars is not expected to have an Earth-like lower mantle composed of bridgmanite and ferropericlase, owing to a much lower pressure (18 to 19 GPa) and temperature (1,900 to 2,000 K) at its core mantle boundary (13). Therefore, the counterpart of the 660-km discontinuity on Earth, arising from the dissociation of ringwoodite to bridgmanite and ferropericlase, is not present within the Martian mantle.

The Clapeyron slopes of these postolivine transitions within Mars are predicted to be positive (25, 28), requiring a shallower (or deeper) transition in a colder (or hotter) mantle. Thus, the depth of the associated seismic discontinuity is a key source of information on the thermal state of the planet. Compositional enrichment of iron (29) or increased water content (30, 31) in the mantle would shift the discontinuity toward shallower depths, mimicking the effects of lower temperature. In addition, the presence of water is found to broaden the postolivine transition (32–34), reducing the sharpness of the seismic discontinuity. Thus, seismic observations of the depth and sharpness of the midmantle discontinuity arising from the postolivine transition provide an invaluable insight into the temperature and composition of the Martian mantle.

Results

Observations of Mantle Triplications on Mars. Earth's MTZ was first discovered by analyzing the behavior of P-wave travel time curves (35). Early studies on MTZ discontinuities utilized refracted waves bottoming above and below the 410- and 660-km depths, forming travel time triplications, and inverted the data from these triplications for one-dimensional (1D) velocity structures of Earth's mantle (36, 37). Here we follow a similar method to identify the P and S triplications that resulted from the interactions with a midmantle discontinuity within Mars using the InSight data (Fig. 1 *A* and *B*). As an example, the predicted travel time curves from a prelanding model (38) exhibit two intersecting triplications (Fig. 1 *C* and *D*): the AB and BC branches are associated with a weak seismic discontinuity from the phase change from orthopyroxene (opx) to high-pressure clinopyroxene (HP-cpx) at ~800 km depth (39), while the CD, DE, and EF branches are related to the seismic discontinuity from the postolivine transition at ~1,000 km depth. Here we simply refer to these two discontinuities as 800 and 1,000. On Earth, the opx to HP-cpx transition provides one possible mechanism to explain the X discontinuity at ~300 km depth, but the lower proportion of opx in Earth's upper mantle at these depths (<10 vol %) compared to the expected Martian mantle (~20 vol %) hinders this phase transition from producing a global discontinuity (39). Our study focuses on the analyses of CD, DE, and EF branches of the predicted triplications to constrain the depth and sharpness of the 1,000 discontinuity which is likely to be associated with the postolivine transitions and subsequently infer the thermal and compositional state of the Martian mantle.

The InSight Marsquake Service (MQS) classifies seismic events into low- and high-frequency families based on their dominant frequency content (9, 10). The low-frequency family, including both low-frequency (LF) and broadband (BB) events,

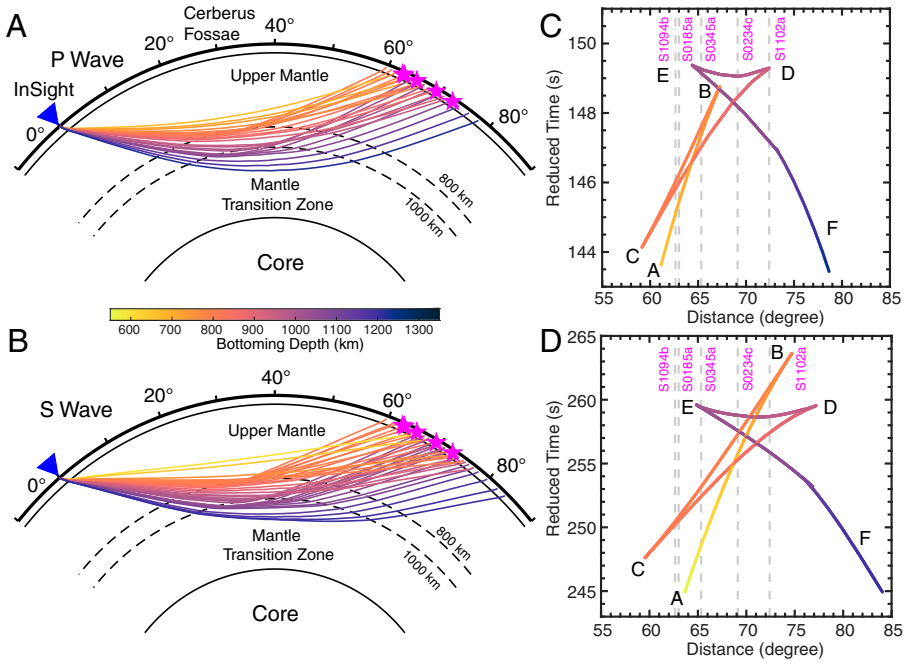

Fig. 1. Ray path geometry and predicted travel times of mantle triplications in Mars. Teleseismic ray paths of (*A*) P waves and (*B*) S waves interacting with the discontinuities in the midmantle, colored according to their bottoming depths. Triplications formed between 60° and 85° from the InSight lander (blue triangle). Pink stars indicate the locations of five LF and BB events which are calculated from $t_S - t_P$ measurements using the EH45coldCrust1 model (38) and assuming a 30-km source depth. Reduced travel time curves (time–distance/velocity) of (*C*) P and (*D*) S triplications predicted from the EH45TcoldCrust1 model. Reduction velocities are 12 and 6.5 km/s for P and S waves, respectively. Branches A to C correspond to triplications from ~800 km depth (associated with the opx to HP-cpx transition), and branches C to F correspond to triplications from ~1,000 km depth (associated with the postolivine transition). The gray dashed lines highlight the epicentral distances of five LF and BB events.

is interpreted as a set of marsquakes that originate in the deep crust or mantle and radiate seismic waves deep into the mantle. In contrast, the high-frequency family is attributed to shallow events with most of their energy trapped in the crust (40). Here we focus on the LF and BB events to search for deep mantle triplications. From the MQS catalog, we down-selected five LF and BB events that have $t_S - t_P$ values (differential travel times between P and S waves) consistent with the 60° to 85° distance range expected for mantle triplications: S0185a, S0234c, S0345a, S1094b, and S1102a (*SI Appendix*, Table S1-1) (41, 42). Among these events, S1094b (~Mw 4) and S1102a (~Mw 3) are the largest events and have energy reaching above 5 Hz, while the other three events are dominated by energy between 0.1 and 1 Hz. Due to crustal scattering, it is not straightforward to pick P and S arrivals directly from the unfiltered seismograms, especially for S0234c and S0345a that have lower signal-to-noise ratios (SNRs). Therefore, we used a polarization filter (43), in addition to a Butterworth bandpass filter (0.3 to 0.9 or 0.5 to 0.9 Hz), to improve the SNR of the P- and S-wave signals, while suppressing signals that are not rectilinearly polarized, such as noise and scattered waves. We also carried out frequency-dependent polarization analysis (FDPA) to validate the vertical polarizations for P waves and horizontal polarizations for S waves (44). All of our P- and S-arrival picks must show consistent vertical or horizontal polarizations from the polarization filter and FDPA methods. Finally, to ensure our picks are not contaminated by wind or pressure changes, we performed a comodulation analysis between the wind/pressure data and seismic data (45). Our analyses only kept P- and S-arrival picks that had excess seismic energy above the environmental noise. The resulting dataset of P- and S-arrival picks was then used to determine the epicentral distances and to search for later-arriving triplicated phases.

To facilitate body wave identifications, we aligned the waveforms on their first P and S arrivals and ordered them by $t_S - t_P$ (Fig. 2). This alignment reveals secondary arrivals following the P and S waves whose travel times are consistent with the predicted move-outs of mantle triplications and, furthermore, have amplitudes and polarities similar to the direct P and S arrivals. One possibility is that these arrivals are depth phases (e.g., pP and sS for a range of event depths), but we rule out this interpretation based on the following lines of evidence: 1) The two event depths obtained from interpreting these arrivals as pP and sS phases from a single event are inconsistent with each other for the examined events. 2) The lack of surface waves and short codas of most events imply these LF and BB events occurred in the deep crust or uppermost mantle (10). If source depths are greater than 30 km, the pP and sS phases are then predicted to arrive later than 12 and 22 s after the first P and S arrivals, respectively (11–13); thus, they are unlikely to interfere with the mantle triplications. 3) Depth phases travel twice through the crust at the source side, thereby losing more energy due to crustal scattering and attenuation (4, 40), and would have overall lower amplitudes than the direct phase regardless of the radiation pattern for the event. Furthermore, for surface events (e.g., a meteoroid impact), we would not expect to observe depth phases at all. We also exclude the possibility that these phases arise from crustal conversions or reflections because these phases would only have amplitudes ~20% of the first P and S waves (47) and would be further suppressed by the polarization filter due to noise contamination (*SI Appendix*, Fig. S4-11). We only observe crustal S reflections from the two large events, S1094b and S1102a, arriving ~10 s after the S wave. These phases do not interfere with the candidate S triplications (*SI Appendix*, Figs. S1-1 and S1-3). With these considerations, we interpret these secondary arrivals as candidate P and S triplications caused by the interactions with the 1,000 discontinuity and investigate their characters further with seismic waveform modeling. We also demonstrate with synthetic modeling that the magnitude thresholds for detecting the P and S triplications are Mw 2.5 (*SI Appendix*, Fig. S4-9) and 3.5 (*SI Appendix*, Fig. S4-10), respectively, compatible with the reported magnitude range (Mw 2.6 to 4.0) for LF and BB events (9, 48), indicating that mantle triplications are detectable by InSight.

Synthetic Waveform Modeling. We used a waveform modeling approach based on a suite of mineral physics-derived radial models for Mars to fit the triplication data and determine the exact depth at which the 1,000 discontinuity occurs (*SI Appendix*, Fig. S2-2). These 1D models are derived from six different mantle compositions [DW85 (14), EH45 (17), KC08 (46), LF97 (15), TAY13 (19), and YM20 (20)] with mantle potential temperatures (T_P) ranging from 1,305 to 1,705 K. We selected a representative subset of 60 models out of a total of ~2,000 models constructed to cover the entire temperature and composition model space. We used the spectral-element code AxiSEM (49) to compute high-frequency synthetic waveforms ($T_{dom} = 2s$) that match the frequency content of the data (0.1 to 1.0 Hz). Since the focal mechanisms and depths of these events are unknown, we assumed a normal faulting source at 30 km depth in the waveform modeling, which is similar to seismic events located at Cerberus Fossae (50). The source depth assumption is supported by a recent body wave study (51) which suggests most high-quality LF and BB events are located at ~30 km depth. Our synthetic tests performed for different focal mechanisms demonstrate that our waveform modeling results are not significantly affected by the assumption of a normal faulting source (*SI Appendix*, Fig. S4-2). Given the similar take-off angles at the source, triplicated waveforms do not have a high sensitivity to focal mechanisms, allowing us to model waveforms using a single source by adjusting polarities accordingly. We aligned the events with the synthetics that have similar $t_S - t_P$ values within the uncertainty range (*SI Appendix*, Table S1-1) using cross-correlations. Correlation coefficients (CCs) between data and synthetics were subsequently calculated to quantify misfits ($misfit = 1 - CC$).

Depth and Sharpness of the 1,000-km Discontinuity. We explored a wide range of candidate mantle compositions and potential temperatures to identify models that matched the observed waveforms (*SI Appendix*, Fig. S1-15). We find two models that show a high correlation match for P (Fig. 2*A*, *mean CC* = 0.73) and S triplications (Fig. 2*B*, *mean CC* = 0.77), respectively. This high consistency between waveform matches supports the identification of these seismic phases as mantle triplications. The waveform modeling was carried out independently for P and S triplications, and each phase showed slightly different sensitivities to the 1,000 depth which were measured at the center depth of the phase transition. The two best-fitting models show consistent T_P values (1,605 K) but different mantle compositions and 1,000 depths: KC08 and 1,013 km for P triplication (Fig. 2*A*) and YM20 and 1,027 km for S triplication (Fig. 2*B*). Triplicated waveforms are less sensitive to mantle composition; this topic is discussed in the next section. The ranges of 1,000 depths consistent with the observed P and S triplications are 994 ± 62 km (Fig. 3 *A* and *C*) and 1,008 ± 49 km (Fig. 3 *B* and *D*), respectively. These P- and S-derived 1,000 depths agree within two SDs; however, as both estimates rely on the same interior structure models, we must address covariance between the two estimates. We therefore computed the total misfit to

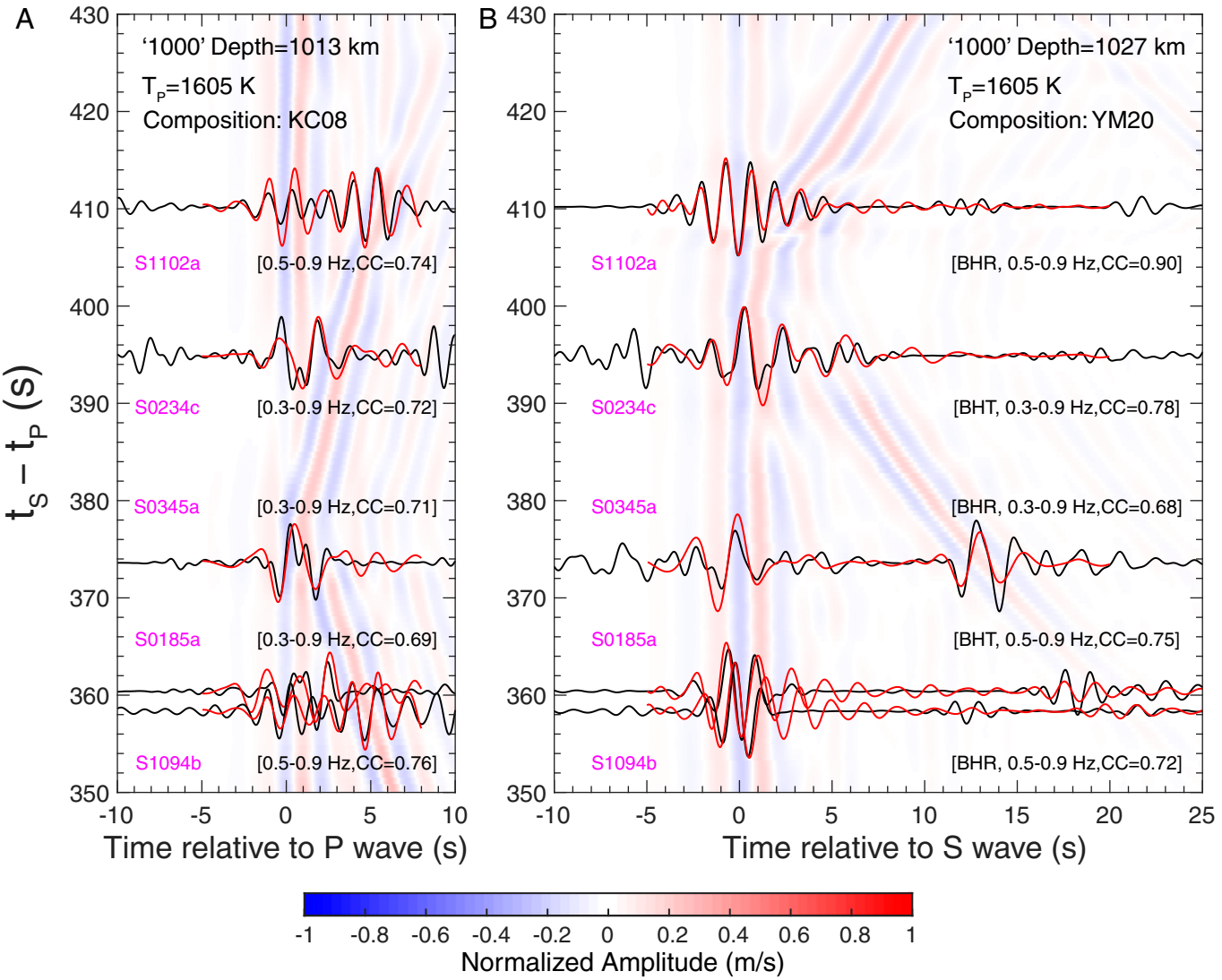

Fig. 2. InSight seismic observations of P and S triplications and synthetic waveform fits. Polarization filtered (*A*) P waveforms on the vertical component (BHZ) and (*B*) S waveforms on the transverse (BHT) or radial (BHR) components are shown in black curves. We selected either the BHT or BHR component based upon the SNR of the S waves. The bandpass filters for each waveform are listed to the right. Red curves denote the synthetic waveforms from the best-fitting models, with the CCs listed to the right. The parameters of the best-fitting models are shown on the top, and KC08 (46) and YM20 (20) represent the assumed composition models. Background colors denote the amplitudes of P-wave synthetics on the BHZ component and S-wave synthetics on the BHT component, assuming a 30-km source depth. We only consider the fits between data and synthetics in specific time windows (−5 to 8 s for P waves and −5 to 20 s for S waves) to avoid contamination from other seismic phases and noise. Note that the time windows for the S waves in S0185a and S1094b events are extended to account for possible later arrivals of triplications.

search for best-fitting models in the overlapping depth range that can explain both triplications. We find a subset of 26 models that provide superior fits to the waveforms with misfits lower than 0.33 (Fig. 3*E*). By averaging these lower misfit models, the 1,000 depth range of the best fitting models is constrained to be 1,006 ± 40 km, and corresponds to $T_P = 1605 \pm 100$ K and temperatures between 1,670 and 1,892 K at the 1,000 depth. A recent study based on autocorrelation analysis of ambient noise suggested a mantle discontinuity in the 1,110 to 1,170 km depth range and interpreted this as the olivine–wadsleyite transition (52), which is considerably deeper than our estimate here. However, a detailed study of transient signals (glitches and spikes) arising from deformation internal to the InSight lander and SEIS instrument package showed that the seismic phase interpreted as a mantle discontinuity in that study is likely a signal processing artifact (53).

The 1,000 depth reported above is based upon the assumption of a 30-km-deep source. However, the source depths of these five events are poorly constrained, and there is a direct trade-off between the source depth and 1,000 depth. By assuming a linear areotherm, surface temperature (220 K), and heat flow (20 mW/m^2), the maximum seismogenic depth for Mars is calculated to be ∼130 km based on a temperature threshold of 1,073 K (54). We would underestimate the 1,000 depth and T_P by up to 33 km and 100 K, respectively, especially if the source depths of our events fall toward the deeper end of the 30 to 130 km depth estimate. Conversely, we would overestimate the 1,000 depth by up to 10 km if the seismic sources are all located near the surface (e.g., a meteoroid impact). Furthermore, if the events are located between 0 and 30 km depth, the depth phases (e.g., sS and pP) could therefore potentially interfere with the mantle triplications. However, we would expect this interference to have limited effects on the constraints of the 1,000 depth because the amplitudes of the depth phases are likely smaller due to crustal scattering, and their rectilinear particle motions could be obscured by mode conversions and scattering in the crust as

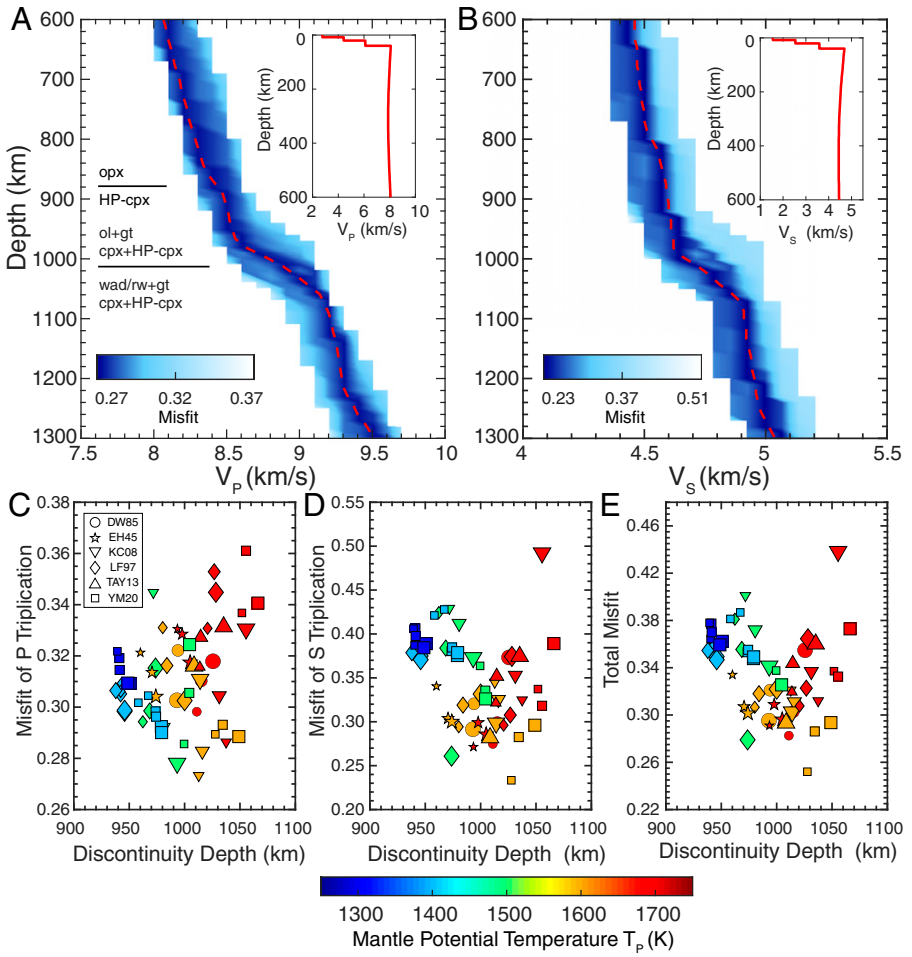

Fig. 3. Depth of the 1,000 discontinuity in Mars from mineral physics and synthetic waveform fits. (*A*) V_P and (*B*) V_S profiles from mineral physics models colored by the misfits of P and S triplications, respectively. Abbreviations for mantle minerals are as follows: olivine (ol), wadsleyite (wad), ringwoodite (rw), garnet (gt), clinopyroxene (cpx), orthopyroxene (opx), and high-pressure clinopyroxene (HP-cpx). The red dashed lines in *A* and *B* highlight the best-fitting models for P and S triplications, respectively. The velocity jump at ~1,000 km depth is associated with the postolivine transition. A shallower minor discontinuity at ~800 km corresponds to the opx to HP-cpx transition. (*Insets*) Crustal and upper mantle structures of the best-fitting model. Misfits of (*C*) P triplication, (*D*) S triplication, and (*E*) total misfits (weighted sum of the misfits of P and S triplications) are shown as a function of the 1,000 discontinuity depth. The colors represent the mantle potential temperature (T_P), and the symbols correspond to six composition models: DW85 (14), EH45 (17), KC08 (46), LF97 (15), TAY13 (19), and YM20 (20). Sizes of the symbols denote the mantle adiabatic gradients: 0.125 K/km (small), 0.15 K/km (medium), and 0.175 K/km (large).

well as noise contamination. Therefore, the interference of depth phases could be effectively suppressed by polarization filtering (*SI Appendix*, Fig. S4-16). Future studies that incorporate detailed inversions of the source depths and focal mechanisms of these five events or more future events could aid in improving the constraints on the 1,000 depth.

Mantle triplications are also sensitive to the sharpness of the 1,000 discontinuity which can be used to constrain the thickness of the postolivine transition. To investigate this, we performed a synthetic waveform sensitivity test by varying the discontinuity thickness between 0 and 200 km in the best-fitting model with lowest total misfit (Fig. 3*B*, where the 1,000 depth was fixed to 1,027 km). We find that the total misfit is minimized when the discontinuity thickness is between 20 and 100 km (*SI Appendix*, Fig. S4-5), corresponding to a pressure interval of 0.76 ± 0.51 GPa. This indicates that the postolivine transition occurs on Mars over a broader depth range compared to the sharp 410-km discontinuity observed on Earth (thickness <10 km or 0.4 GPa) (55). We also investigate the existence of opx to HP-cpx transition by removing the 800 discontinuity in the best-fitting model (Fig. 3*B*) and then repeating our waveform modeling. We find that the total misfit increased slightly from 0.25 to 0.26 after removing the relatively subtle discontinuity produced by the opx to HP-cpx transition (*SI Appendix*, Fig. S4-6), indicating the boundary plays a negligible role in the waveform fits. More seismic events from Mars will be required to reach any conclusion on the nature of opx to HP-cpx phase transition.

Discussion

The ranges of the 1,000 discontinuity depth and thickness are consistent with predictions for the postolivine transition from mineral physics (Fig. 4). Therefore, we prefer to ascribe the 1,000 discontinuity to the postolivine transition for further interpretations of the mantle temperature and composition of Mars, even though we cannot completely rule out the possibility of a compositional change or other boundaries at this depth. Our estimates of the mantle potential temperature shed light on the thermal state of the interior and provide important constraints for the thermal evolution of Mars. The mineral physics models that fit the range of the 1,000 depth (1,006 ± 40 km) indicate a relatively cold Martian mantle compared to pre-InSight mission constraints (Fig. 4*A*), although the temperature estimate is consistent with T_P values (1,600 to 1,700 K) inferred from the inversions for upper mantle structure of Mars that used

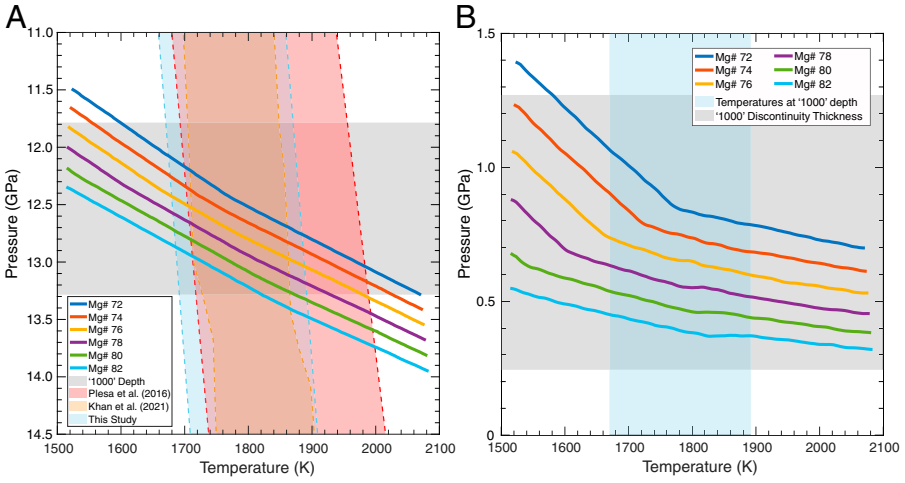

Fig. 4. Implications for the temperature and bulk composition of Martian mantle. (*A*) Depths of postolivine transitions are shown as a function of temperature. Note that the depths are converted to corresponding pressures using the density profiles. Solid lines in color represent the phase boundaries between olivine and wadsleyite/ringwoodite for various Mg # [molar Mg/(Mg + Fe) × 100%]. These phase boundaries were derived using the temperature and pressure at the center depth of the phase transition. The gray shaded region represents the observed range of 1,000 depth and corresponding pressures. The colored shaded regions denote the mantle temperature profiles inferred from premission estimates (pink) (56), upper mantle structures (orange) (12), and this study (blue). The dashed lines highlight the upper and lower bounds of these temperature profiles. (*B*) Thicknesses of postolivine transitions for various Mg # models, which are measured along the isentrope, are shown as a function of temperature. The phase transition thicknesses are converted to the corresponding pressure intervals using the density profiles. Note that the slope change is associated with the switch from olivine–ringwoodite to olivine–wadsleyite transitions as temperature increases. The gray shaded region indicates the constrained range of discontinuity thickness (60 ± 40 km or 0.76 ± 0.51 GPa) from mantle triplications. The blue shaded region shows the constrained temperature range (1,670 to 1,892 K) at the 1,000 depth.

InSight data (12). Our T_P estimate also agrees well with the temperatures suggested by the geochemical analysis of surface volcanic rocks of Amazonian age (1,643 ± 40 K) (57). The T_P estimate presented here is colder than the values derived from shergottites, which are relatively young Martian rocks with ages of 180 and 472 Ma (1,753 ± 10 K and 1,823 ± 10 K, respectively) (58). This suggests that the T_P estimates obtained from the analysis of shergottites may not be representative of the average mantle but rather are associated with thermal anomalies, potentially indicating the presence of localized mantle upwellings or plumes within the interior of Mars in recent geological history. The latter may be responsible for volcanic activity in provinces such as Tharsis and Elysium up to the recent past that has been suggested by young lava flows observed in these regions (59, 60).

Although the postolivine transition is primarily sensitive to temperature, it is also affected by the bulk mantle composition and presence of volatiles. The 1,000 depth increases with Mg # [molar Mg/(Mg + Fe) × 100%; Fig. 4*A*], whereas Mg/Si ratio and refractory elements have little to no effect on the 1,000 depth (*SI Appendix*, Fig. S5-1). The 26 models that showed the lowest overall total misfit (Fig. 3*E*) are based on six different bulk compositions proposed in the literature (i.e., DW85, EH45, KC08, LF97, TAY13, and YM20), for which Mg # varies between 73 and 79. We tested the effects of composition in more detail by using DW85 model as a basis and creating compositional models by mixing chondritic compositions (61) to expand the Mg # range to 72 to 82. Given the trade-off between temperature and composition, as well as large uncertainties on temperature (±100 K), it is not possible to fully constrain Mg # from the range of the 1,000 depth alone (Fig. 4*A*). Multiple mantle compositions are thus permissible by the limited P and S triplications we observed here (Fig. 3*E*). Compared to temperature, the lower sensitivities of the 1,000 depth and seismic velocities to mantle composition as well as its trade-off with temperature hinder the possibility of distinguishing among composition models from seismic observations alone (62).

As the phase transition thickness decreases with increasing Mg # and temperature (Fig. 4*B*), our observation of a broad 1,000 discontinuity (~0.76 GPa) supports the notion that the Martian mantle is more iron-rich than Earth's mantle. We note that the seismic discontinuity thickness can underestimate the phase transition thickness when most of the phase transitions only occur within a small width of the phase loop (63, 64). Here all composition models satisfy the range of phase transition thickness given the constrained range of temperatures at the 1,000 depth. Further constraints on mantle composition could be obtained by detailed inversions of both depth and sharpness of the 1,000 discontinuity from the triplicated waveforms.

Mantle hydration could also potentially affect the depth and sharpness of the postolivine transition. Due to the large water solubility in wadsleyite and ringwoodite (up to ~3.1 wt %) (65) relative to olivine (up to ~0.9 wt %) (66), the addition of water expands the stability field of wadsleyite to lower pressure, broadening and shallowing the postolivine transition. However, thermodynamic modeling (*SI Appendix*, Fig. S5-4) suggests that although the onset pressure of the postolivine transition may decrease by >1 GPa at high bulk water contents (>3,000 ppm), the majority of the phase transition would take place at only slightly lower pressures (~0.2 GPa). Coupled with the 70 to 300 ppm concentrations of water in Martian mantle estimated from shergottite, nakhlite and chassignite (SNC) meteorites (67, 68), we suggest that water is unlikely to have a major effect on the seismically observed 1,000 depth. Therefore, considering the trade-offs with mantle temperature and bulk composition as well as the large uncertainty of the 1,000 depth, our observations cannot add further constraints on the water content of Martian mantle.

By combining our seismic observations with geodynamic modeling, we can further constrain the mantle composition and the initial thermal state as well as the mantle rheology that is compatible with the observed 1,000 depth range and reconstruct the thermochemical history of Mars. Following this approach (69), we find that among the five main composition models proposed for Mars (TAY13, LF97, YM20, KC08, and EH45), only the EH45 and KC08 compositions appear to be compatible with the 1,000 depth range of 1,006 ± 40 km (*SI Appendix*, Fig. S3-2). Although the YM20 composition yields

the best-fit for P and S triplications (Fig. 3*E*), the geodynamic models derived from this composition, which satisfy the MoI and present-day crustal constraints, are mostly deeper than the upper bound of the 1,000 depth (*SI Appendix*, Fig. S3-2). Since different crustal density structures could allow for a modest shift in the 1,000 depth toward shallower values in the accepted range, the YM20 composition would remain marginally compatible with the observed 1,000 depths. Our modeling results imply a relatively sluggish mantle (reference viscosity $10^{20.4}$ to $10^{21.7}$ Pa s) that had a moderately cold uppermost convective mantle temperature 4.5 Gy ago (<1,850 K). The models also indicate that the resulting crust is 10 to 15 times more enriched in heat-producing elements relative to the primitive mantle, in agreement with gamma ray spectrometer data (70). In addition, the geodynamic models predict present-day surface heat flow to be 21 to 24 mW/m^2. These ranges agree with inversions for the upper mantle structure of Mars from InSight (12) and premission estimates (7, 69).

The InSight measurement of the 1,000 depth reported here is notably a regional measurement, although averaged over multiple events, and may not necessarily represent the global Martian average mantle. However, the observed mantle is not expected to deviate significantly from the rest of the planet (7). The traces of relatively recent volcanism at the surface of Mars (59, 60) suggest that thermal heterogeneity may be present within the mantle and could potentially create topography and lateral variations on the 1,000 discontinuity, similar to those observed on Earth. Ultimately, the measurement of the 1,000 depth is an important constraint for updating and formulating geochemical and planetary evolution models. The detection of additional marsquakes during the extended InSight mission and other future seismological investigations would expand our understanding of the details of the Mars' deep mantle, including an improved constraint on the 1,000 discontinuity thickness, presence of other seismic discontinuities in close proximity to the postolivine transition (71), regional lateral variations in discontinuity depth that are diagnostic fingerprints of thermal and chemical heterogeneities (72), and the presence of water and other mantle volatiles (58).

Methods

Polarization Filter. Seismic events on Mars are often characterized by strong scattered waves as well as wind noise (4), thereby complicating the identifications of body waves. Here we used a polarization filtering technique to enhance rectilinearly polarized waves such as P and S waves, while suppressing other nonrectilinearly polarized waves including background noise or scattered waves. This technique is particularly useful to remove the noise with the same frequency content as the body waves. A polarization filter was previously applied to the detections of core-reflected phases in the Apollo seismic data (73) as well as surface-reflected waves (12, 74) and core phases (13) on Mars. We followed the method by Montalbetti and Kanasewich (43) to design a time-domain polarization filter for improving the SNR of teleseismic P and S waves. First, we computed the covariance matrix of the three-component data (R, T, Z) in a given time window (5 s) around t_0 and the eigenvectors and eigenvalues of this matrix. The rectilinearity at time t_0 is defined as the following equation:

$$RL(t_0) = \left[1 - \left(\frac{\lambda_2}{\lambda_1}\right)^n\right]^J, \quad [1]$$

where λ_1 and λ_2 are the largest and second largest eigenvalues, respectively, and n and J are the empirical exponents. The eigenvector of the principal axis is $\vec{E} = (e_1, e_2, e_3)$ with respect to the R, T, Z coordinate system. The direction function on each component at time t_0 is given by

$$D_i(t_0) = e_i^K, \quad [2]$$

where i = 1, 2, 3 (R, T, Z) and K is the empirical exponent. We chose these empirical values for the exponents: $n = 0.5$, J = 1, and K = 2 (43). The polarization filter for each component is defined as the product of rectilinearity and the corresponding direction function. The filtered three-component seismograms at any time t are given by

$$R_f(t) = R(t) \cdot RL(t) \cdot D_R(t), \quad [3]$$

$$T_f(t) = T(t) \cdot RL(t) \cdot D_T(t), \quad [4]$$

$$Z_f(t) = Z(t) \cdot RL(t) \cdot D_Z(t). \quad [5]$$

FDPA. We applied FDPA on waveforms of our five LF/BB events used in the analysis. This method has been previously implemented to detect and identify the core-reflected ScS phases on Mars (13). To summarize, we computed the S transform of three component waveforms recorded by InSight SEIS Very Broadband (VBB) and obtained a 3 × 3 cross-spectral covariance matrix in 90% overlapping time windows whose duration varies inversely with frequency. The relative sizes of the eigenvalues of this covariance matrix are related to the degree of polarization of the particle motion, while the complex-valued components of the eigenvectors describe the particle motion ellipsoid in each time–frequency window (44). We focused on when the particle motion of our seismic signal was rectilinear so we could effectively describe the orientation of the particle motion with the inclination and azimuth. To pick the direct P and S arrivals in our seismic records, we used a pair of metrics that can emphasize horizontally (HRM) and vertically rectilinear motion (VRM) and searched for those arrivals whose average HRM or VRM across different frequencies were high (see more details in the supplement of ref. 13).

Comodulation Analysis. In this section we adopt the comodulation analysis described in ref. 45 to evaluate the contributions of environmental signals into the seismic records and thus aid discrimination between weather-induced noise and seismic energy for each of the candidate mantle triplication events. Comodulation evaluates the correlation in signal power between the measured environmental variables (wind and pressure) and ground motion. It has been demonstrated particularly successful in identifying seismic energy that is in excess of the expected noise injected from the local weather (9, 45, 75).

The comodulation approach uses the method of moments to match the mean and variance of the seismic and environmental signals prior to the start time of the putative marsquake. We first estimate these first two moments for all signals for a total of 15 min prior to the marsquake event and remove the effect of any identified glitches in the record which contaminate the statistical moments. The method of moments is then used to match the mean and variance of the seismic acceleration and pressure rms envelopes to the measured wind speed signal. The seismic rms envelope is estimated as the total power of all three combined Z, N, and E components. Both seismic and pressure rms envelopes are extracted in discrete half-octave frequency bands with center frequencies from 1/26.5 up to 6.8 Hz, with the last frequency bin extending up to the anti-alias filter (8 Hz) of the continuous 20 samples per second VBB data.

In this approach, comodulation shows that the envelopes of the seismic power continuously track the pressure envelopes and wind speed, and therefore, any divergence from the expected noise match can then be interpreted as being from a seismic source. Each of the candidate events in the manuscript for mantle triplications located at epicentral distances between 60° and 85° is henceforth evaluated with respect to the comodulation analysis. For events that do not have weather data due to lander power constraints after sol 700, highly sensitive lander resonances excited by the wind and atmospheric phenomena are used as proxies for atmospheric noise injection (45, 76).

Data Processing Steps and Phase Identification. Marsquakes are broadly classified as two families: 1) low-frequency (LF) and 2) high-frequency (HF) events based on their frequency content (9, 10). The dominant energy of LF events is below 1 Hz, while some events have more broadband energy extended above 1 Hz, which are classified as a subgroup: broadband (BB) events. The HF events have energy mostly above 1 Hz and can extend up to 6 to 12 Hz (40). MQS ranks these events from quality A to D (A being the highest quality) based on the clarity and polarization of the phases (9). In this study, we focused on the LF and BB events that travel deep into the mantle to search for triplications from the MTZ. We have identified five LF and BB events with $t_S - t_P$ values that cause

them to fall in the target distance range for triplications: S1094b (*SI Appendix*, Fig. S1-1), S1102a (*SI Appendix*, Fig. S1-3), S0185a (*SI Appendix*, Fig. S1-5), S0234c (*SI Appendix*, Fig. S1-7), and S0345a (*SI Appendix*, Fig. S1-9).

We first removed the instrument response from the data to transfer seismograms to velocity, and the three SEIS VBB components were rotated from UVW configuration to the ZNE coordinate frame (8). Then, we band pass filtered the seismogram between 0.3 and 0.9 or 0.5 and 0.9 Hz to remove long-period noise and high-frequency resonances and eliminate the 1-Hz tick noise resulting from cross-talk between the temperature sensors and SEIS VBB seismometers (77). The choices of band pass filters are informed by the comodulation analysis and filter banks: we used the 0.5 to 0.9 Hz filter for the events (e.g., S1102a) that do not have clear excess seismic energy below 0.5 Hz; otherwise, we used the 0.3 to 0.9 Hz filter. We first applied polarization filtering in the ZNE coordinate to pick the P arrival of each event on the vertical component (BHZ) based upon the MQS reported start time of seismic energy (9). We then compared our picks to the FDPA results to examine the vertical polarizations for P waves (e.g., *SI Appendix*, Fig. S1-1*A*). We only picked the arrivals when these two methods show consistent peak energy, then assigned the uncertainties to include both peaks. To obtain event back-azimuth, we computed the average principal axis of P-wave particle motions, which is expressed as $\vec{P} = (P_E, P_N, P_Z)$, using a 5-s time window centered around the P wave. The back-azimuth of the event is then calculated using the following equation (e.g., ref. 78):

$$BAZ = arctan\left(\frac{P_E}{P_N}\right) + \pi. \quad [6]$$

We used the P-wave–derived back-azimuth to rotate the horizontal components (BHN and BHE) to radial (BHR) and transverse (BHT) components. The event back-azimuths are summarized in *SI Appendix*, Table S1-1. However, due to the low amplitudes of P waves, the back-azimuths are often not well constrained, so we examined both the BHR and BHT components for our S-wave triplication study.

After rotation, we applied the polarization filter, now in the ZTR coordinate system, to pick the S arrivals with the guidance of MQS reported picks. Ideally, we would prefer to pick S arrival on the transverse component to avoid P to S converted phases. However, since the back-azimuths are poorly constrained, we picked S arrivals on both radial and transverse components and only kept the pick with the larger SNR. For example, the S wave of S1094b event is two times larger on the radial component than the transverse component (*SI Appendix*, Fig. S1-1*B*). Therefore, we picked this S arrival on the radial component. Similarly to P wave, we compared our S-arrival picks to the horizontal polarizations from FDPA to ensure these two methods show consistent peak energy within the uncertainty range (e.g., *SI Appendix*, Fig. S1-1*B*). All the P- and S-arrival picks were made at the maximum amplitudes of the polarization filtered envelopes. Finally, we examined our P- and S-arrival picks using the comodulation analysis: both picks must show excess energy above the environmental noise (e.g., *SI Appendix*, Fig S1-2); otherwise, they were discarded from our analysis. For example, we identified two other events (S0167a and S0167b) that are located in the distance range appropriate for mantle triplications, but their P waves do not show any excess energy (*SI Appendix*, Figs. S1-11 and S1-12). Therefore, we excluded these two events from our analysis due to the wind contamination. We repeated the same picking processes for the other four candidate events (*SI Appendix*, Figs. S1-3–S1-10). We calculated the SNR of P and S waves as the ratio between the maximum envelope and the average envelope amplitude in a noise time window (−150 to −50 s before P arrival). P waves typically have smaller SNRs between 2 and 7, whereas S waves show larger SNR between 3 and 51 (*SI Appendix*, Table S1-1).

SEIS is deployed on the surface of Mars where a harsh environment inevitably causes artifacts in the data. Although SEIS is protected under the wind and thermal shield, the daily internal temperature variations can still reach up to 15 K. The thermal variations lead to one type of instrument self-noise manifested as large amplitude deviations over a short time period, hereafter referred to as a "glitch". A typical SEIS glitch appears as a large one-sided pulse accompanied by high-frequency spikes near the onset (79). We highlight some large glitches in *SI Appendix*, Figs. S1-1–S1-10, and they often appear as very broadband energy on the spectrogram. We avoided these known glitches identified by MQS during our phase picking by excluding any picks that fell within ±20s of a glitch signal (e.g., *SI Appendix*, Fig. S1-5). As informed by comodulation analysis, we also excluded the time windows that were contaminated by wind noise or pressure change (e.g., *SI Appendix*, Fig. S1-1).

Synthetic Waveform Modeling. We derived a suite of seismic structure models based on six composition models [DW85 (14), EH45 (17), KC08 (46), LF97 (15), TAY13 (19), and YM20 (20)] with mantle potential temperature T_P ranging from 1,300 to 1,700 K (see *Structure Models of Mars* for more details). We propagated synthetic seismic waves through these seismic structure models to simulate the waveforms of triplications for comparison with the data. We used the spectral element code AxiSEM (49) to generate synthetics with a dominant period of 2 s. The focal mechanisms and depths of these five triplication events are unknown, but the three Cerberus Fossae events (S0173a, S0235b, and S0183a) were constrained to have normal faulting sources between 33 and 40 km depth (50). Therefore, we assumed a similar tectonic setting for these five LF and BB events and selected a normal faulting source at 30 km for the waveform modeling. Note that a trade-off exists between the source depth and 1,000 depth (e.g., increasing the source depth by X km would cause the 1,000 depth to be ∼X/3 km deeper). We chose a moment tensor to allow for seismic energy in the receiver direction from all three types of waves: P wave, SH wave, and SV wave (*SI Appendix*, Fig. S1-13). The receivers were placed on the equator from 55° to 85° with a 0.1° spacing (5.9 km). We artificially increased the crustal attenuation ($Q_\mu = Q_\kappa = 10$) to suppress the crustal conversions and reverberations after P and S arrivals, while the mantle attenuation was muted ($Q_\mu = Q_\kappa = 10^5$) to keep the high-frequency content of the triplicated waveforms. We suppressed the crustal phases as they likely vary between our observed events and are unconstrained in the models. In addition, we demonstrated that the polarization filtering can suppress the crustal phases in the data due to their low amplitudes, especially for events with lower SNR like S0234c and S0345a (*SI Appendix*, sections 4.5 and 4.6). We used these tests to ensure that the waveform modeling fits are not biased by crustal phases in both the data and the synthetics.

To show the characteristics of triplicated waveforms, we present six example models from our model space that span the range of possible 1,000 depths (938 to 1,066 km). We aligned the synthetics on the first P and S arrivals and ordered them by $t_S - t_P$ in the same way as we did with the observed seismic data (*SI Appendix*, Fig. S1-14). Triplicated waveforms display a K shape of travel time move-out after the alignment on P or S arrivals. The $t_S - t_P$ values at the center of the triplications generally increase with the 1,000 depth (or T_P). We observe crustal reverberations after the P wave on the vertical component (*SI Appendix*, Fig. S1-14*A*) and after the S wave on the radial component (*SI Appendix*, Fig. S1-14*C*), whereas the transverse component mostly contains triplications (*SI Appendix*, Fig. S1-14*B*). S to P conversions arrive ∼5 s before the first S arrival on the radial component (*SI Appendix*, Fig. S1-14*C*). These crustal phases also exhibit triplications but have much smaller amplitudes than the first P and S arrivals, thereby only contributing minimal misfits to the waveform modeling. Depth phases pP and sS are expected to arrive ∼12 and 22 s after the P and S waves, respectively, but they are eliminated in the synthetics as a result of the strong attenuation in the crustal model.

After computing the synthetics, we used them to interpret the triplicated waveforms. Since the epicentral distances of these events are unknown, we matched the synthetics and data based on $t_S - t_P$ values. For each event, we searched through the synthetics within the ± 5 s uncertainty range of $t_S - t_P$ measurement (*SI Appendix*, Table S1-1) to find the best-fitting synthetic waveform. As the uncertainties of $t_S - t_P$ vary from the events, we also tested ±7.5 and ±10 s uncertainties for the waveform modeling. We obtained similar results despite using different uncertainties, thereby retaining the ±5 s uncertainty range for the waveform modeling. We only investigated the vertical component for P triplication. Due to the less well-constrained back-azimuth, there is uncertainty in the horizontal rotation of the events. Therefore, we used both transverse and radial components for S triplication but only kept the one with a lower misfit. As the focal mechanisms of these events are unconstrained, we tested both positive and negative polarities for each synthetic waveform and again kept the one with a lower misfit. During the waveform modeling, we applied the following data processing steps for each synthetic waveform. 1) We normalized the amplitudes of the data and synthetics to unity. 2) We cut a time window around the first P and S arrivals: −5 to 8 s for P wave (*SI Appendix*, Fig. S1-15*A*) and −5 to 20 s for S wave (*SI Appendix*, Fig S1-15*B*). S0185a and S1094b events required extended time windows to account for possible later arrivals of S triplications. We used −5 to 30 s for the S waves of S0185a and S1094b events (*SI Appendix*, Fig. S1-15*B*). 3) We aligned the cut synthetics with the data using a cross-correlation

method. 4) Finally, we computed the normalized CCs between the data $d(x,t)$ and synthetic waveforms $u(x,t)$ using the following equation (80):

$$CC = \frac{\int \mathrm{d(x,t)} \cdot \mathrm{u(x,t)dt}}{\sqrt{\int |\mathrm{d(x,t)}|^2 dt \cdot \int |\mathrm{u(x,t)}|^2 dt}}. \quad [7]$$

We only kept the synthetics with the largest CC for each event in a given model. We then computed the mean value of CC in each model as follows:

$$\overline{CC} = \frac{\sum_{i=1}^{N} CC_i}{N}, \quad [8]$$

where N represents the number of events ($N = 5$). We define the misfit function for each model using the following equation:

$$\chi = 1 - \overline{CC}. \quad [9]$$

We computed the weighted sum of the misfits of P and S triplications as the total misfits:

$$\chi_{total} = (\chi_P + 2\chi_S)/3, \quad [10]$$

where χ_P and χ_S are the misfits of P and S triplications, respectively. We assigned a weighting factor of two to S triplications because the time window length for S triplication is about two times longer than P triplications, and the SNR of S waves are generally larger.

Here we show six example waveform modeling results from our model space (*SI Appendix*, Fig. S1-15). The synthetic waveforms are plotted on top of the data for direct comparisons. Misfits of S triplications (*SI Appendix*, Fig. S1-15*A*) show larger variations as a function of the 1,000 depth compared to P triplication (*SI Appendix*, Fig. S1-15*B*). Both misfits are minimized in the intermediate 1,000 depth range (1,000 to 1,030 km). In our model space, we found 26 models that can simultaneously fit both P and S triplications, including our best-fitting model ($T_P = 1,605\ K$, YM20).

Structure Models of Mars

We have built a suite of elastic models of Mars for the waveform modeling of triplications. The models were calculated along the areotherms (mantle temperature profiles) created using an error function profile with an added linear gradient,

$$T(z) = T_0 + T_m \mathrm{erf}\left(\frac{z}{\sqrt{\kappa t}}\right) + z\left(\frac{dT}{dz}\right)_{adiabatic}, \quad [11]$$

where T_0 is the surface temperature, which was set to 205 K; t is the age, which was set to 4.25×10^9 y; κ is the thermal diffusivity, which was set to 10^{-6} m^2/s; T_m took values of 1,100, 1,200, 1,300, 1,400, and 1,500 K; and $\left(\frac{dT}{dz}\right)_{adiabatic}$ is the thermal gradient of mantle adiabatic and took values of 0.125, 0.150, and 0.175 K/km. The error function term is used to approximate the temperature structure in the lithosphere, while the linear term accounts for the adiabatic increase in temperature with depth in the convecting mantle, plus a component of subadiabaticity/superadiabaticity. Mantle potential temperature was calculated as $T_P = T_0 + T_m$. This produced 15 different areotherms. All parameters were held constant through the crust, mantle, and core. All of these areotherms have heat flows less than 15 mW/m^2. A summary figure of the areotherms used in the construction of the structure models is given in *SI Appendix*, Fig. S2-1.

We used the three-layer crust model beneath the InSight lander constrained from receiver functions and ambient noise (11). The V_P and V_S values in the three-layer crust are shown in *SI Appendix*, Table S2-1. The densities for the crust were calculated from Birch's law (81):

$$\rho = (V_P + 1.87)/0.00305, \quad [12]$$

where V_P is given in km/s. For layer 1, 30% porosity is assumed, and for layers 2 and 3, 0% porosity is assumed.

The mantle was divided into 100 equally spaced divisions as a function of radius. Six different mantle compositions were explored [DW85 (14), EH45 (17), KC08 (46), LF97 (15), TAY13 (19), and YM20 (20)]. Stable phases were calculated for bulk chemistries given as oxide weight percentages in *SI Appendix*, Table S2-1 by Gibbs free energy minimization using PerpleX (82), and the thermodynamic database of ref. 83, with temperatures ranging from 205 to 2,500 K and pressure ranging from 500 to 510,000 bars. So-obtained tables were converted into BurnMan readable materials (84). Each of the resulting models was then input as a BurnMan mantle material. Along with the crust and core, these were input into BurnMan's planet class.

The core was divided into 20 equally spaced divisions as a function of radius. The core models were created based on the Elastic Parameters of the Outer Core (EPOC) model by ref. 85, which fit an isentropic Vinet equation of state for the core to the Earth's normal mode data. Irving et al. (85) suggest that the EPOC core model (which is presented in terms of molar volume, m^3/mol) would be a useful starting point for other planetary cores. We used a molar mass of 39 to 42 g/mol, which gives core densities in the middle of the range of other models. Irving et al. (85) used 50 g/mol for Earth's core. Varying the core molar mass will increase or decrease the core density. For each of the mantle compositions in *SI Appendix*, Table S2-2, the radius of the core–mantle boundary was varied from 1700 km to 1850 km in 2 km increments. The mass of the planet and MoI coefficient were monitored, and models with a total mass of the planet within 2% of the planetary mass (6.4185×10^{23} kg) and 0.2% of the MoI coefficient (0.36379) from ref. 86 are shown in *SI Appendix*, Fig. S2-2. These loose restrictions were used to allow the widest possible range of compositions and temperatures to be considered. We selected a subset of the models with a core radius close to 1,830 km, which is consistent with the seismic observations from core-reflected waves (13). This subset includes 60 models and covers all six composition models and the entire mantle potential temperature range (1,305 to 1,705 K). We used these models to model the waveforms of triplications and constrain the 1,000 depth (*Synthetic Waveform Modeling*).

Geodynamic Modeling of Thermochemical Evolution of Mars

We investigated the conditions that are compatible with the observations of 1,000 depths reported in this study by modeling the thermochemical evolution of a Mars-like planet via a parameterized approach. The method is described in detail elsewhere (69, 87) and will therefore only be briefly summarized below.

Our approach consists of computing the thermal and chemical transfers in a spherically symmetric planet of radius R = 3,389.5 km composed of several concentric envelopes: a liquid adiabatic iron-alloy core, a convecting silicate mantle, overlaid by an evolving lithospheric lid that includes an evolving crust enriched in heat-producing elements (HPE) with respect to the mantle. Each evolution differs in the value of several governing parameters that were varied within plausible bounds (*SI Appendix*, Table S3-1): the mantle rheology (its activation energy [E^*], activation volume [V^*], and its viscosity [η_0] at reference pressure P_{ref} = 3 GPa and temperature T_{ref} = 1,600 K), the crustal enrichment factor (Λ) defined as the ratio of heat production in the crust to the bulk silicate production, the initial uppermost

mantle temperature (Tm_0), the initial core–mantle boundary temperature (Tc_0), and the core radius (Rc).

We considered five main distinct bulk silicate compositions in terms of major elements and HPE contents (U, Th, and K; *SI Appendix*, Table S3-2): KC08 (46), TAY13 (19), LF97 (15), EH45 (17), and YM20 (20). Bulk mantle properties (density, thermal expansion, and specific heat) resulting from the composition were considered. Each thermochemical history (corresponding to a given set of aforementioned model parameters) evolves for 4.5 Gyr. The resulting thermochemical structure is then used to compute the seismic velocity structure at the present day. In the mantle, our mineralogical model relies on the Perple_X Gibbs energy minimization software (82) with the thermodynamic database of ref. 88. For the core, we used the model of ref. 38 in which the density is adjusted to match the mass constraint on Mars, $M = 6.417 \times 10^{23} \pm 2.981 \times 10^{19}$ kg (86). In the crust, the seismic velocity and density are based on the results of receiver functions, while the crustal density is iteratively adjusted within bounds compatible with receiver functions and gravity data inversion (11).

We require that the computed thermochemical histories 1) are compatible with estimates of Mars' normalized MoI factor $I/(MR^2) = 0.36340 \pm 0.0006$, 2) are compatible with estimates of the degree-2 Love number $k_2 = 0.174 \pm 0.008$ that includes an atmospheric correction (89), 3) have present-day crustal thickness (Dcr) lying within the bounds inferred from receiver functions and gravity data, Dcr = 39 to 72 km (11), and 4) have a present-day lithosphere thicker than 500 km (in which we include the uppermost mantle thermal boundary layer because seismic velocity gradients due to radial temperature changes remain large in this region), as suggested by seismic data (12). Models that fail to satisfy these four constraints are rejected. Similarly, evolutions that result in subcritical mantle Rayleigh numbers (i.e., nonconvecting mantles) are rejected in order to be compatible with the recent traces of volcanism observed at the surface of Mars (90, 91). The models account for lithospheric and crustal evolution, which involves either growth or recycling. In particular, if the deep lithosphere thins, it can in some cases trigger crustal recycling (92).

For the models that satisfy all the above constraints, we searched for the occurrence of postolivine (ol-wd) and opx to HP-cpx transitions. These depths are determined based on the occurrence of S-wave seismic velocity jumps rather than on the appearance of the mineralogical phases, which is not necessarily accompanied by a velocity change and therefore would not produce triplications. We considered a mantle seismic velocity variation as a seismic jump if the local Vs gradient $|dVs/dr|$ is larger than three times the mean Vs gradient value averaged over the mantle. We detected the two transitions by searching for such occurrences in the depth ranges 600 to 900 km for the opx to HP-cpx transition and 900 to 1,300 km for the postolivine transition.

SI Appendix, Fig. S3-1 illustrates the results of this search for two distinct evolutions. Even though both cases share the same bulk mantle composition, the values of the other governing parameters are different, yielding distinct thermochemical evolutions and present-day thermal and seismic structures. One case shown (*SI Appendix*, Fig. S3-1 *A–C*) yields a relatively cold present-day mantle, while the other (*SI Appendix*, Fig. S3-1 *D–F*) results instead in a relatively hot mantle at present day. This difference in temperature structure leads to the occurrence of both postolivine and opx to HP-cpx transitions in the cold case, while only the postolivine transition is visible in the hot case. This indicates that the relationships between the occurrence of mantle transitions and the planet structure, bulk composition, and initial state can be exploited to reconstruct the planet's history and to constrain the value of several present-day characteristics. To do so, we sampled the parameter space defined in *SI Appendix*, Table S3-1 in order to search for thermochemical evolutions that are compatible with current constraints from seismic, gravity, and geodetic data listed above with constraints from the present study on mantle transition depths.

Thermal histories that are compatible with present-day crustal thicknesses in the range 39 to 72 km and with lithospheric thicknesses larger than 500 km are displayed in *SI Appendix*, Fig. S3-2 for the five Martian compositions considered. They represent a small subset (i.e., <1%) of the parameter space (listed in *SI Appendix*, Table S3-1) consisting of 10^5 randomly sampled models per composition considered. The panels in *SI Appendix*, Fig. S3-2 represent four present-day output quantities: the surface heat flow, the crustal enrichment factor, and the depths of the postolivine and opx to HP-cpx transitions. Thermal histories that satisfy the current state of Mars (displayed in light blue) yield distinct ranges of surface heat flow and crustal enrichment for different compositions. This essentially results from the fact that each composition has a distinct HPE content (*SI Appendix*, Table S3-2). Compositions with enriched HPE contents lead to hotter evolutions, yielding larger amounts of shallow melting and crustal extraction and therefore thicker crusts (and thinner lithospheres) and vice versa. The average value of crustal enrichment Λ = 10 to 15 is similar among the five compositions and is compatible with surface estimates from gamma ray spectrometer data (70). One should note, however, that several compositions yield considerably fewer compatible evolutions compared to others. For example, the TAY13 composition has only eight compatible evolutions (*SI Appendix*, Fig. S3-2 *E–H*). This primarily reflects the impact of mantle composition combined with crustal thickness on the planet MoI. As shown in ref. 11, the TAY13 composition is hardly compatible with the MoI constraint, while the YM20 composition is the most compatible with the MoI requirements. In addition, we observe a poor compatibility of the LF97 composition (*SI Appendix*, Fig. S3-2 *M–P*). The latter is due to the fact that the high enrichment in heat-producing elements for this composition yields either too much crustal production (hence crustal thickness above the acceptable range) or lithospheres that are too thin (<500 km) to be compatible with seismic data (11, 12).

To further constrain the parameter space, we considered the evolutions that are compatible with the occurrence of at least the postolivine transition within the depth range of 1,006 ± 40 km, as inferred from the analysis of seismic data presented in this study. The corresponding cases are displayed in medium blue in *SI Appendix*, Fig. S3-2 and reveal that despite the fact that the YM20 composition was the most compatible with current constraints, it yields no evolution that matches the postolivine depth constraint. Similarly, the TAY13 and LF97 compositions yield postolivine transition depths that are deeper than the acceptable range. In contrast, EH45 and KC08 are the only compositions that show evolutions compatible with postolivine depth constraints (*SI Appendix*, Fig. S3-2 *C* and *S*). *SI Appendix*, Tables S3-3 and S3-4 summarize the values of the governing parameters and the corresponding values of several present-day quantities that are compatible with constraints on postolivine transitions for the EH45 and KC08 compositions, respectively. These characteristics are compatible with other recent postlanding predictions (11, 12) and are in line with prelanding thermal-orbital constraints on the Mars–Phobos evolution (69) and with several earlier premission estimates (7, 21, 56, 92, 93).

Overall, when combining the current state of Mars with the constraints on the 1,000 depth and geodynamic considerations, our results favor the EH45 and KC08 bulk compositions. This leads to a crustal enrichment factor of 10 to 15 and a present-day average surface heat flow of 21 to 24 mW/m^2. These compositions are associated with a relatively sluggish mantle (reference viscosity $10^{20.4}$ to $10^{21.7}$ Pa s) and an initially moderately cold mantle (Tm_0 = 1,720 to 1,859 K). Such characteristics are broadly compatible with previous estimates.

Data, Materials, and Software Availability. The InSight seismic data (42) have been deposited in the Institut de Physique du Globe de Paris (IPGP) data center (https://doi.org/10.18715/SEIS.INSIGHT.XB_2016). These data are also available from Incorporated Research Institutions for Seismology (IRIS) Data Management Center (DMC), NASA Planetary Data System (PDS), and SEIS-InSight data portal.

ACKNOWLEDGMENTS. We thank the editor and two anonymous reviewers for their constructive comments. We acknowledge NASA; Centre National D'Etudes Spatiales (CNES); their partner agencies and Institutions (UK Space Agency [UKSA], Swiss Space Office [SSO], German Aerospace Center [DLR], Jet Propulsion Laboratory [JPL], IPGP–National Center for Scientific Research [CNRS], Eidgenössische Technische Hochschule Zürich [ETHZ], Imperial College [IC], and Max Planck Institute for Solar System Research [MPS-MPG]); and the flight operations team at JPL, SeIS on Mars Operations Center [SISMOC], Mars SEIS Data Service [MSDS], IRIS-DMC, and PDS for providing SEED SEIS data and mission support. This paper is InSight Contribution 203. Q.H., N. C. Schmerr, D.K., R.R.M., and F.K. acknowledge the funding from NASA grant 80NSSC18K1628 and NASA Solar System Exploration Research Virtual Institute (SSERVI) Cooperative Agreement 80NSSC19M0216. Q.H. and L.W. were supported by NSF grant EAR-1853662. Q.H. and E.B. acknowledge NASA grant 80NSSC18K1680. V.L. was supported by a Packard Foundation Fellowship. S.D.K. acknowledges NASA grant 80NSSC18K1623. A.R. was financially supported by the Belgian PROgramme for the Development of scientific EXperiments (PRODEX) program managed by the European Space Agency in collaboration with the Belgian Federal Science Policy Office. M.C. and A.-C.P. acknowledge the financial support and endorsement from the DLR Management Board Young Research Group Leader Program and the Executive Board Member for Space Research and Technology. R.M. was supported by a UKSA Aurora Research Fellowship (ST/R001332/1). D.A. and N. C. Siersch have received funding from the European Research Council under the European Union's Horizon 2020 research and innovation program (grant agreement 724690). D.A. also acknowledges the support by CNES, focused on the SEIS instrument of the InSight mission. M.B., C. Bollinger, F.B., and C.M. acknowledge the CNES funding and Agence Nationale de la Recherche (ANR) MArs Geophysical InSight (MAGIS) (ANR-19-CE31-0008-08). T.G. acknowledges a government contract of the Schmidt Institute of Physics of the Earth, Russian Academy of Sciences. C. Beghein acknowledges NASA grant 80NSSC18K1679. J.C.E.I. acknowledges Science and Technology Facilities Council (STFC)/UKSA grant ST/W002515/1. A.H. was supported by STFC/UKSA Aurora grants ST/R002096/1 and ST/W002523/1. B.F., K.L., and T.N.-M. were supported by STFC/UKSA Aurora grant ST/S001379/1. M.P.P., S.E.S., and W.B.B were supported by the funding from JPL under a NASA contract (80NM0018D0004).

Author affiliations: [a]Department of Geology, University of Maryland, College Park, MD 20742; [b]Department of Geophysics, Colorado School of Mines, Golden, CO 80401; [c]Department of Geosciences, Virginia Polytechnic Institute and State University, Blacksburg, VA 24061; [d]Institute of Geophysics, ETH Zurich, 8092 Zurich, Switzerland; [e]Royal Observatory of Belgium, 1180 Brussels, Belgium; [f]Institute of Planetary Research, German Aerospace Center, 12489 Berlin, Germany; [g]Institut de Physique du Globe de Paris, Université de Paris, CNRS, 75005 Paris, France; [h]Istituto Nazionale di Geofisica e Vulcanologia, Sezione di Bologna, 40128 Bologna, Italy; [i]Department of Electrical and Electronic Engineering, Imperial College London, London SW7 2AZ, United Kingdom; [j]School of Earth Sciences, University of Bristol, Bristol BS8 1RJ, United Kingdom; [k]Institut de Minéralogie, de Physique des Matériaux et de Cosmochimie, Sorbonne Université, Muséum National d'Histoire Naturelle, UMR CNRS 7590, 75005 Paris, France; [l]Institut Supérieur de l'Aéronautique et de l'Espace, 31400 Toulouse, France; [m]Institut de Recherche en Astrophysique et Planétologie, Université Toulouse III Paul Sabatier, CNRS, 31062 Toulouse, France; [n]Laboratoire de Géologie de Lyon–Terre, Planètes, Environnement, Université de Lyon, École Normale Supérieure de Lyon, Université Claude Bernard Lyon 1, CNRS, Lyon, 69007 France; [o]Schmidt Institute of Physics of the Earth, Russian Academy of Sciences, Moscow 123242, Russia; [p]Department of Earth Sciences, University of Oxford, Oxford OX1 3AN, United Kingdom; [q]Department of Earth, Planetary, and Space Sciences, University of California, Los Angeles, CA 90095; [r]Physical Sciences Group, James Cook University, Douglas, QLD 4811, Australia; [s]Max Planck Institute for Solar System Research, 37077 Göttingen, Germany; [t]Black Forest Observatory, Stuttgart University, 77709 Wolfach, Germany; and [u]Jet Propulsion Laboratory, California Institute of Technology, Pasadena, CA 91109

Author contributions: Q.H., N. C. Schmerr, S.D.K., D.K., A.R., A.-C.P., H.S., V.L. designed research; N. C. Schmerr, E.B., and L.W. acquired funding; Q.H., N. C. Schmerr, S.D.K., D.K., A.R., A.-C.P., H.S., R.R.M., F.K., C.C., M.C., R.M., D.A., M.D., M.B., C. Bollinger, C.M., T.G., J.C.E.I., A.H., B.F., K.L., T.N.-M., F.B., and N. C. Siersch performed research; Q.H., D.K., R.R.M., F.K., C.C., J.-R.S., P.M.D., P.L., B.P., R.W.-S., and W.T.P. analyzed data; Q.H., N. C. Schmerr, S.D.K., D.K., A.R., A.-C.P., H.S., R.R.M., F.K., V.L., C.C., M.C., R.M., D.A., M.B., C.M., J.C.E.I., E.B., C. Beghein, L.W., and N. C. Siersch wrote the paper; P.L., M.P.P., S.E.S., T.S., W.T.P., D.G., and W.B.B. managed the InSight Mission.

1. A. N. Halliday, H. Wänke, J.-L. Birck, R. N. Clayton, The accretion, composition and early differentiation of Mars. *Space Sci. Rev.* **96**, 197–230 (2001).
2. P. Lognonné, B. Mosser, Planetary seismology. *Surv. Geophys.* **14**, 239–302 (1993).
3. W. B. Banerdt *et al.*, Initial results from the InSight mission on Mars. *Nat. Geosci.* **13**, 183–189 (2020).
4. P. Lognonné *et al.*, Constraints on the shallow elastic and anelastic structure of Mars from InSight seismic data. *Nat. Geosci.* **13**, 213–220 (2020).
5. W. B. Banerdt *et al.*, "InSight: A discovery mission to explore the interior of Mars" in *44th Lunar and Planetary Science Conference* (2013), vol. 1719, p. 1915.
6. M. P. Panning *et al.*, Planned products of the Mars structure service for the InSight mission to Mars. *Space Sci. Rev.* **211**, 611–650 (2017).
7. S. E. Smrekar *et al.*, Pre-mission InSights on the interior of Mars. *Space Sci. Rev.* **215**, 3 (2019).
8. P. Lognonné *et al.*, SEIS: InSight's seismic experiment for internal structure of Mars. *Space Sci. Rev.* **215**, 12 (2019).
9. J. F. Clinton *et al.*, The Marsquake catalogue from InSight, sols 0–478. *Phys. Earth Planet. Inter.* **310**, 106595 (2021).
10. D. Giardini *et al.*, The seismicity of Mars. *Nat. Geosci.* **13**, 205–212 (2020).
11. B. Knapmeyer-Endrun *et al.*, Thickness and structure of the Martian crust from InSight seismic data. *Science* **373**, 438–443 (2021).
12. A. Khan *et al.*, Upper mantle structure of Mars from InSight seismic data. *Science* **373**, 434–438 (2021).
13. S. C. Stähler *et al.*, Seismic detection of the Martian core. *Science* **373**, 443–448 (2021).
14. G. Dreibus, H. Wänke, Mars, a volatile-rich planet. *Meteoritics* **20**, 367–381 (1985).
15. K. Lodders, B. Fegley, An oxygen isotope model for the composition of Mars. *Icarus* **126**, 373–394 (1997).
16. J. W. Morgan, E. Anders, Chemical composition of Mars. *Geochim. Cosmochim. Acta* **43**, 1601–1610 (1979).
17. C. Sanloup, A. Jambon, P. Gillet, A simple chondritic model of Mars. *Phys. Earth Planet. Inter.* **112**, 43–54 (1999).
18. F. Sohl, T. Spohn, The interior structure of Mars: Implications from SNC meteorites. *J. Geophys. Res.* **102**, 1613–1635 (1997).
19. G. J. Taylor, The bulk composition of Mars. *Chem. Erde* **73**, 401–420 (2013).
20. T. Yoshizaki, W. F. McDonough, The composition of Mars. *Geochim. Cosmochim. Acta* **273**, 137–162 (2020).
21. A. Khan *et al.*, A geophysical perspective on the bulk composition of Mars. *J. Geophys. Res.* **123**, 575–611 (2018).
22. A.-C. Plesa *et al.*, The thermal state and interior structure of Mars. *Geophys. Res. Lett.* **45**, 12,198–12,209 (2018).
23. F. Xu *et al.*, Low velocity zones in the Martian upper mantle highlighted by sound velocity measurements. *Geophys. Res. Lett.* **48**, e2021GL093977 (2021).
24. C. M. Bertka, Y. Fei, Mineralogy of the Martian interior up to core-mantle boundary pressures. *J. Geophys. Res.* **102**, 5251–5264 (1997).
25. J. Ita, L. Stixrude, Petrology, elasticity, and composition of the mantle transition zone. *J. Geophys. Res.* **97**, 6849–6866 (1992).
26. A. E. Ringwood, *Composition and Petrology of the Earth's Mantle* (McGraw-Hill, New York, 1975).
27. K. E. Bullen, Seismology and the broad structure of the earth's interior. *Phys. Chem. Earth* **1**, 68–93 (1956).
28. T. Katsura, E. Ito, The system Mg_2SiO_4-Fe_2SiO_4 at high pressures and temperatures: Precise determination of stabilities of olivine, modified spinel, and spinel. *J. Geophys. Res.* **94**, 15663–15670 (1989).
29. Y. Fei, C. M. Bertka, "Phase transitions in Earth's mantle and mantle mineralogy" in *Mantle Petrology: Field Observations and High-Pressure Experimentation: A Tribute to F. R. Boyd* (1999). Y. Fei, C. M. Bertka, B. O. Mysen. Oxford University Press.
30. J. Chen, T. Inoue, H. Yurimoto, D. J. Weidner, Effect of water on olivine-wadsleyite phase boundary in the (Mg,Fe)2SiO4 system. *Geophys. Res. Lett.* **29**, 1875 (2002).
31. J. R. Smyth, D. J. Frost, The effect of water on the 410-km discontinuity: An experimental study. *Geophys. Res. Lett.* **29**, 123–1–123-4 (2002).
32. B. J. Wood, The effect of H_2O on the 410-kilometer seismic discontinuity. *Science* **268**, 74–76 (1995).
33. D. J. Frost, D. Dolejš, Experimental determination of the effect of H_2O on the 410-km seismic discontinuity. *Earth Planet. Sci. Lett.* **256**, 182–195 (2007).
34. V. N. Zharkov, T. v. Gudkova, Seismic model of Mars: Effects of hydration. *Planet. Space Sci.* **104**, 270–278 (2014).
35. P. Byerly, The Montana earthquake of June 28, 1925, G.M.C.T. *Bull. Seismol. Soc. Am.* **16**, 209–265 (1926).
36. M. Niazi, D. L. Anderson, Upper mantle structure of western North America from apparent velocities of *P* waves. *J. Geophys. Res.* **70**, 4633–4640 (1965).
37. S. P. Grand, D. v. Helmberger, Upper mantle shear structure of North America. *Geophys. J. R. Astron. Soc.* **76**, 399–438 (1984).
38. A. Rivoldini, T. van Hoolst, O. Verhoeven, A. Mocquet, V. Dehant, Geodesy constraints on the interior structure and composition of Mars. *Icarus* **213**, 451–472 (2011).
39. A. B. Woodland, The orthorhombic to high-P monoclinic phase transition in Mg-Fe pyroxenes: Can it produce a seismic discontinuity? *Geophys. Res. Lett.* **25**, 1241–1244 (1998).

40. M. van Driel *et al.*, High-frequency seismic events on Mars observed by InSight. *J. Geophys. Res.* **126**, e2020JE006670 (2021).
41. InSight Marsquake Service, Mars Seismic Catalogue, InSight Mission, v. 9 2022-01-01.(ETHZ, IPGP, JPL, ICL, Univ. Bristol, 2022). http://www.insight.ethz.ch/seismicity/catalog/v9. Accessed 1 January 2022.
42. InSight Mars SEIS Data Service, SEIS Raw Data, Insight Mission. (IPGP, JPL, CNES, ETHZ, ICL, MPS, ISAE-Supaero, LPG, MFSC, 2019). https://datacenter.ipgp.fr/networks/detail/XB_2016. Accessed 1 January 2019.
43. J. F. Montalbetti, E. R. Kanasewich, Enhancement of teleseismic body phases with a polarization filter. *Geophys. J. R. Astron. Soc.* **21**, 119–129 (1970).
44. J. Park, F. L. Vernon, C. R. Lindberg, Frequency dependent polarization analysis of high-frequency seismograms. *J. Geophys. Res.* **92**, 12664–12674 (1987).
45. C. Charalambous *et al.*, A comodulation analysis of atmospheric energy injection into the ground motion at InSight, Mars. *J. Geophys. Res.* **126**, e2020JE006538 (2021).
46. A. Khan, J. A. D. Connolly, Constraining the composition and thermal state of Mars from inversion of geophysical data. *J. Geophys. Res.* **113**, 7003 (2008).
47. D. Kim *et al.*, Improving constraints on planetary interiors with PPs receiver functions. *J. Geophys. Res.* **126**, e2021JE006983 (2021).
48. M. Böse *et al.*, Magnitude scales for marsquakes calibrated from InSight data. *Bull. Seismol. Soc. Am.* **111**, 3003–3015 (2021).
49. T. Nissen-Meyer *et al.*, AxiSEM: Broadband 3-D seismic wavefields in axisymmetric media. *Solid Earth* **5**, 425–445 (2014).
50. N. Brinkman *et al.*, First focal mechanisms of marsquakes. *J. Geophys. Res.* **126**, e2020JE006546 (2021).
51. C. Durán *et al.*, Seismology on Mars: An analysis of direct, reflected, and converted seismic body waves with implications for interior structure. *Phys. Earth Planet. Inter.* **325**, 106851 (2022).
52. S. Deng, A. Levander, Autocorrelation reflectivity of Mars. *Geophys. Res. Lett.* **47**, e2020GL089630 (2020).
53. D. Kim *et al.*, Potential pitfalls in the analysis and structural interpretation of seismic data from the Mars InSight mission. *Bull. Seismol. Soc. Am.* **111**, 2982–3002 (2021).
54. A.-C. Plesa *et al.*, Present-day Mars' seismicity predicted from 3-D thermal evolution models of interior dynamics. *Geophys. Res. Lett.* **45**, 2580–2589 (2018).
55. H. M. Benz, J. E. Vidale, Sharpness of upper-mantle discontinuities determined from high-frequency reflections. *Nature* **365**, 147–150 (1993).
56. A. C. Plesa *et al.*, How large are present-day heat flux variations across the surface of Mars? *J. Geophys. Res.* **121**, 2386–2403 (2016).
57. D. Baratoux, M. J. Toplis, M. Monnereau, O. Gasnault, Thermal history of Mars inferred from orbital geochemistry of volcanic provinces. *Nature* **472**, 338–341 (2011).
58. J. Filiberto, R. Dasgupta, Constraints on the depth and thermal vigor of melting in the Martian mantle. *J. Geophys. Res.* **120**, 109–122 (2015).
59. J. Vaucher *et al.*, The morphologies of volcanic landforms at Central Elysium Planitia: Evidence for recent and fluid lavas on Mars. *Icarus* **200**, 39–51 (2009).
60. E. Hauber, P. Brož, F. Jagert, P. Jodłowski, T. Platz, Very recent and wide-spread basaltic volcanism on Mars. *Geophys. Res. Lett.* **38**, L10201 (2011).
61. J. T. Wasson, G. W. K. Allemeyn, Compositions of chondrites. *Philos. Trans. R. Soc. Lond. A* **325**, 535–544 (1988).
62. C. Houser, J. W. Hernlund, J. Valencia-Cardona, R. M. Wentzcovitch, Discriminating lower mantle composition. *Phys. Earth Planet. Inter.* **308**, 106552 (2020).
63. J. W. Hernlund, On the interaction of the geotherm with a post-perovskite phase transition in the deep mantle. *Phys. Earth Planet. Inter.* **180**, 222–234 (2010).
64. L. Stixrude, Structure and sharpness of phase transitions and mantle discontinuities. *J. Geophys. Res.* **102**, 14835–14852 (1997).
65. T. Inoue, H. Yurimoto, Y. Kudoh, Hydrous modified spinel, Mg1.75SiH0.5O4: A new water reservoir in the mantle transition region. *Geophys. Res. Lett.* **22**, 117–120 (1995).
66. J. R. Smyth, D. J. Frost, F. Nestola, C. M. Holl, G. Bromiley, Olivine hydration in the deep upper mantle: Effects of temperature and silica activity. *Geophys. Res. Lett.* **33**, 15301 (2006).
67. F. M. McCubbin *et al.*, Hydrous melting of the Martian mantle produced both depleted and enriched shergottites. *Geology* **40**, 683–686 (2012).
68. F. A. Weis *et al.*, Water content in the Martian mantle: A Nakhla perspective. *Geochim. Cosmochim. Acta* **212**, 84–98 (2017).
69. H. Samuel, P. Lognonné, M. Panning, V. Lainey, The rheology and thermal history of Mars revealed by the orbital evolution of Phobos. *Nature* **569**, 523–527 (2019).
70. W. V. Boynton *et al.*, Concentration of H, Si, Cl, K, Fe, and Th in the low- and mid-latitude regions of Mars. *J. Geophys. Res.* **112**, 12–99 (2007).
71. A. Deuss, J. H. Woodhouse, A systematic search for mantle discontinuities using SS-precursors. *Geophys. Res. Lett.* **29**, 90–94 (2002).
72. T. R. A. Song, D. V. Helmberger, S. P. Grand, Low-velocity zone atop the 410-km seismic discontinuity in the northwestern United States. *Nature* **427**, 530–533 (2004).
73. R. C. Weber, P. Y. Lin, E. J. Garnero, Q. Williams, P. Lognonné, Seismic detection of the lunar core. *Science (1979)* **331**, 309–312 (2011).
74. Q. Huang, *Investigating the Internal Structure of Earth and Mars with Seismic Body Waves* (University of Maryland, College Park, 2020).
75. S. Ceylan *et al.*, Companion guide to the Marsquake catalog from InSight, Sols 0–478: Data content and non-seismic events. *Phys. Earth Planet. Inter.* **310**, 106597 (2021).
76. N. L. Dahmen *et al.*, Resonances and lander modes observed by InSight on Mars (1–9 Hz). *Bull. Seismol. Soc. Am.* **111**, 2924–2950 (2021).
77. N. Compaire *et al.*, Autocorrelation of the ground vibrations recorded by the SEIS-InSight seismometer on Mars. *J. Geophys. Res.* **126**, e2020JE006498 (2021).
78. J. R. Scholz *et al.*, Orienting ocean-bottom seismometers from P-wave and Rayleigh wave polarizations. *Geophys. J. Int.* **208**, 1277–1289 (2017).
79. J. R. Scholz *et al.*, Detection, analysis, and removal of glitches from InSight's seismic data from Mars. *Earth Space Sci.* **7**, 215 (2020).
80. K. Tao, S. P. Grand, F. Niu, Full-waveform inversion of triplicated data using a normalized-correlation-coefficient-based misfit function. *Geophys. J. Int.* **210**, 1517–1524 (2017).
81. F. Birch, Composition of the Earth's mantle. *Geophys. J. Int.* **4**, 295–311 (1961).
82. J. A. D. Connolly, Computation of phase equilibria by linear programming: A tool for geodynamic modeling and its application to subduction zone decarbonation. *Earth Planet. Sci. Lett.* **236**, 524–541 (2005).
83. L. Stixrude, C. Lithgow-Bertelloni, Thermodynamics of mantle minerals–II. Phase equilibria. *Geophys. J. Int.* **184**, 1180–1213 (2011).
84. S. Cottaar, T. Heister, I. Rose, C. Unterborn, BurnMan: A lower mantle mineral physics toolkit. *Geochem. Geophys. Geosyst.* **15**, 1164–1179 (2014).
85. J. C. E. Irving, S. Cottaar, V. Lekić, Seismically determined elastic parameters for Earth's outer core. *Sci. Adv.* **4**, eaar2538 (2018).
86. A. S. Konopliv, R. S. Park, W. M. Folkner, An improved JPL Mars gravity field and orientation from Mars orbiter and lander tracking data. *Icarus* **274**, 253–260 (2016).
87. H. Samuel *et al.*, The thermo-chemical evolution of Mars with a strongly stratified mantle. *J. Geophys. Res.* **126**, e2020JE006613 (2021).
88. L. Stixrude, C. Lithgow-Bertelloni, Thermodynamics of mantle minerals–I. Physical properties. *Geophys. J. Int.* **162**, 610–632 (2005).
89. A. S. Konopliv *et al.*, Detection of the chandler wobble of Mars from orbiting spacecraft. *Geophys. Res. Lett.* **47**, e2020GL090568 (2020).
90. W. K. Hartmann *et al.*, Evidence for recent volcanism on Mars from crater counts. *Nature* **397**, 586–589 (1999).
91. G. Neukum *et al.*; HRSC Co-investigator Team, Recent and episodic volcanic and glacial activity on Mars revealed by the High Resolution Stereo Camera. *Nature* **432**, 971–979 (2004).
92. A. Morschhauser, M. Grott, D. Breuer, Crustal recycling, mantle dehydration, and the thermal evolution of Mars. *Icarus* **212**, 541–558 (2011).
93. S. A. Hauck, R. J. Phillips, Thermal and crustal evolution of Mars. *J. Geophys. Res.* **107**, 5052 (2002).